# Equation of state of liquid mercury to 520 K and 7 GPa from acoustic velocity measurements

S. Ayrinhac, M. Gauthier, L. E. Bove, M. Morand, G. Le Marchand, F. Bergame, J. Philippe, and F. Decremps

# Equation of state of liquid mercury to 520 K and 7 GPa from acoustic velocity measurements

S. Ayrinhac,[1] M. Gauthier,[1] L. E. Bove,[1,2] M. Morand,[1] G. Le Marchand,[1] F. Bergame,[1]
J. Philippe,[1] and F. Decremps[1]

[1]*Institut de Minéralogie, de Physique des Matériaux, et de Cosmochimie (IMPMC), Sorbonne Universités -
UPMC Univ. Paris 06, UMR CNRS 7590, Muséum National d'Histoire Naturelle, IRD UMR 206,
4 Place Jussieu, F-75005 Paris, France*
[2]*Ecole Polytech. Fed. Lausanne, Inst. Condensed Matter Phys., EPSL, CH-1015 Lausanne, Switzerland*

Ultrafast acoustics measurements on liquid mercury have been performed at high pressure and temperature in a diamond anvil cell using picosecond acoustic interferometry. We extract the density of mercury from adiabatic sound velocities using a numerical iterative procedure. We also report the pressure and temperature dependence of the thermal expansion, isothermal and adiabatic compressibility, bulk modulus, and pressure derivative of the latter up to 7 GPa and 520 K. We finally show that the sound velocity follows a scaling law as a function of density in the overall measured metallic state. © 2014 AIP Publishing LLC. [http://dx.doi.org/10.1063/1.4882695]

## I. INTRODUCTION

As far as concerns its thermodynamic properties liquid mercury can be essentially described as a simple liquid,[1] though it is a very unusual element compared to other close-shell elements. As an example, it is the only metal which is liquid at ambient conditions due to relativistic effects on the core electrons,[2,3] and it exhibits anomalous electronic properties[4] compared to other transition metals.

In fact, liquid mercury undergoes a gradual metal non-metal (M-NM) transition when the density decreases below $9 \times 10^3$ kg/m³. Below this density the 6s and 6p bands do no longer overlap and the system loses its metallic character.[5] This transition has been largely investigated, both theoretically and experimentally.[6] In particular, the transition results in an abrupt change of the density dependence of the sound velocity. This change is related to a modification of the interatomic interaction.[7,8] From a general point of view, the relationship between this interatomic potential and the sound velocity is not straightforward as in the corresponding crystal. In the latter case, at 0 K, the sound velocity can be obtained from a simple development of the potential energy of the solid around the equilibrium position of each atom. Similarly, the temperature variation of the sound velocity can be derived from standard anharmonic corrections to this energy.[9] Conversely, such a method cannot be used for the adiabatic speed of sound of a liquid. One can always take, as a reference state, a structure obtained by a rapid and deep quench of the corresponding liquid into an amorphous solid, followed by its local equilibration. A development of the potential energy in a way similar to the ordered case will then result in a "frozen" speed of sound. Nevertheless this speed may have little to do with the actual adiabatic speed of sound of the liquid if the system is in a relaxing regime, i.e., if the probed frequencies are much smaller than $1/\tau_D$, where $\tau_D$ is the characteristic diffusion time for the liquid.[10]

Experimental information on the density dependence of the sound velocity for liquid metals formed of heavy ions, such as mercury,[10] or bismuth,[11] over a large range of pressure and temperature can suggest new approximations in the formulation of the problem or in the building of appropriate interatomic pseudo-potentials. In particular, at large densities, it is the repulsive part of the interatomic potential which mainly determines the adiabatic speed of sound, while the long range electron screened interaction dictates the unrelaxed sound velocity value.[10]

In order to test these ideas, this paper presents new data on liquid mercury sound velocity in a very broad density range (up to 75% variation in the metallic state) on different isotherms. Mercury is a very suitable system to this scope by virtue of its very low melting point and high compressibility which allow to probe large $T/T_m$ and $P/P_0$ conditions, where $T_m$ is the melting temperature and $P_0$ is the ambient pressure. Nevertheless, data on liquid mercury under high compression conditions are scarce and limited to 1.2 GPa,[12,13] due to the technical difficulty to measure sound velocity and density at high pressure. To overcome this lack, numerous analytical representations of the equation of state (EOS) have been proposed. They allow to extrapolate the density measurements carried out at moderate pressures.[12,14] However, different representations often lead to inconsistent results[15] and the effectiveness of such analytical predictions needs to be validated against experimental high pressure data.

In this paper, we report detailed measurements of the sound velocity of liquid mercury along six isotherms from ambient pressure up to a maximum pressure corresponding to the crystallization of the system. Section II details the experimental conditions and the instrumental set-up. The picosecond acoustics technique[16–20] is coupled with a surface imaging method[21–23] in order to extract the sound velocity at each given thermodynamic point. Details of the technique and of the two different methods employed to measure the

sound velocity are given in Secs. III A and III B. The nu-
merical procedure[12,24,25] used to extract the density values is
described in Sec. IV A and Sec. IV B presents the results
and associated thermodynamic data tables. The comparison
of our results with the prediction of the EOS, as derived by
the most commonly used empirical equations, is discussed in
Sec. IV C. Finally, in Sec. V, we plot the experimental veloc-
ity as a function of density and we show that, in the metallic
state, it follows a simple power law with only second order
effects coming from temperature or pressure variations. The
sound velocity functional on density is compared with the pre-
dictions of the Bohm-Staver (BS) model[26] for liquid metals
and with the charged hard sphere (CHS) model.[27]

## II. EXPERIMENTAL SET-UP

The experimental set-up used in this work is shown in
Fig. 1. The light source is a femtosecond Ti:sapphire laser de-
livering $\lambda = 800$ nm light pulses of about 100 fs width, at a
repetition rate of 79.66 MHz. The output of this pulse laser
is splitted into a pump and a probe beams. The pump beam
is modulated at the frequency of 1 MHz by an acousto-optic
modulator. A lock-in amplifier synchronized with the modu-
lation frequency is used to improve the signal-to-noise ratio.
The pump is focused onto a small spot (3 $\mu$m) of the sample
which creates a sudden and small temperature rise of about
1 K. The corresponding thermal stress generated by thermal
expansion relaxes by launching a longitudinal acoustic strain
field mainly along the direction perpendicular to the flat par-
allel faces of the sample. The probe beam is delayed with re-
spect to the pump through a 1 m long delay line used in a four
pass geometry allowing a total temporal range of 13.333 ns
with 1 ps step. The probe beam is focused on a spot on the
surface of the sample opposite to the pump beam.

The time variation of the sample reflectivity is detected
through the variation of the intensity of the reflected probe
beam. This variation is due to thermal and acoustic effects
which both alter the optical reflectivity. The photo-elastic
and the photo-thermal coefficients contribute to the change

of both the imaginary and real parts of the reflectivity,[28]
whereas the surface displacement only modifies its imaginary
part. These changes are detected by a stabilized Michelson
interferometer.[29] A 100 × 100 $\mu$m surface imaging of the
sample can be done by a scan of the probe objective mounted
on a 2D translational motor.

A membrane diamond anvil cell (DAC) is used as the
high pressure generator (see inset of Fig. 1). The pressure is
determined by the shift of the $SrB_4O_7$:5%$Sm^{2+}$ fluorescence
line which is known to be temperature independent[30] with an
accuracy of 0.1 GPa. To reach high temperatures, the DAC is
placed in a resistive furnace. The temperature measurements
were calibrated with the well-known melting line of Hg[31] and
checked by a thermocouple glued on the diamond. The rela-
tive uncertainty on the temperature is estimated to be around
1%. The maximum temperature is limited by our heating ap-
paratus and the breakdown of the objectives close to the heat
source.

Ultra-pure mercury (99.99%) from Alfa Aesar was used
during the whole set of experiments. The gasket material was
rhenium, known to be chemically inert at high temperature
with mercury.[32] Moreover, no reaction is expected to take
place between carbon (i.e., diamond) and mercury.[33] A small
droplet of liquid mercury was loaded in a 200 $\mu$m diameter
hole drilled into a gasket of 50 $\mu$m thickness. A large diame-
ter hole is here chosen to avoid acoustic reflections from the
edges of the gasket. At each given temperature, measurements
were performed by decreasing the pressure from the corre-
sponding melting point to ambient pressure $P_0$.

## III. SOUND VELOCITY MEASUREMENTS

### A. The temporal method

In this first series of measurements, a peak in the reflec-
tivity is observed when the acoustic waves reach the sample
surface opposite to the pump beam incidence surface (see
Fig. 2(a)). Note that, since liquid mercury is fully embed-
ded into the gasket hole, the peak-echo arises at a time $\Delta t$
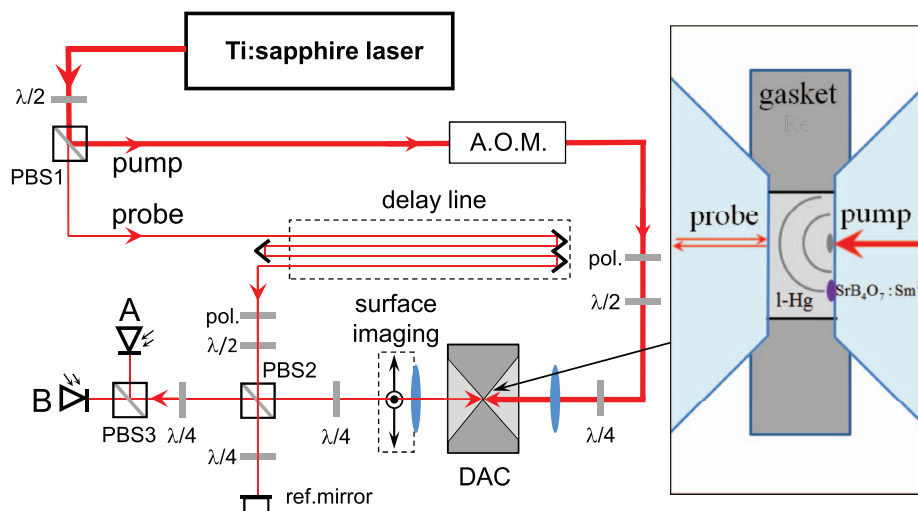


FIG. 1. Schematic set-up of the picosecond acoustics experiment involving a surface imaging set-up and a Michelson interferometer. The inset shows the sample in the DAC with the pump and probe on the opposite sides. PBS: polarizing beam-splitter; $\lambda/4$: quarter wave plate; $\lambda/2$: half-wave plate; pol.: linear polarizer; A.O.M.: acousto-optic modulator. See text for the details.
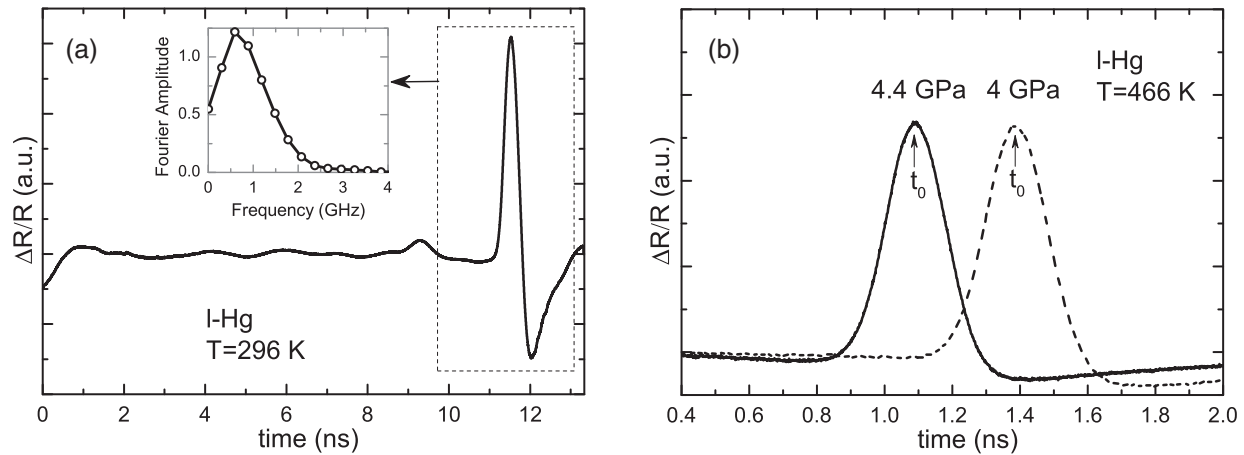
FIG. 2. (a) Variation of reflectivity as a function of time with collinear pump and probe beams focused on the opposite sides of the sample, at ambient pressure. The signal inside the dashed box corresponds to the main acoustic wavefront arriving at the diamond/mercury interface. (Inset) Fourier transform of this echo. (b) Shift of the peak position $t_0$ with pressure.

corresponding to a single travel flight path of the acoustic wave into mercury.

For each pressure and temperature conditions, longitudinal acoustic echoes have been systematically observed. Figure 2(b) illustrates the temporal shift between two acoustic echoes corresponding to two different pressures for a fixed temperature.

The sound velocity $v$ as a function of pressure was derived here from the recorded signal through the use of the following Eq. (1):

$$ v = \frac{e_0}{\Delta t} = \frac{e_0}{t_0 + nT_{laser} - \tau}, \qquad (1) $$

where $e_0$ is the gasket thickness (note that here, the subscripted "0" indicates that the measurement is carried out with a particular and fixed spatial position of the probe, namely, in the axis of the pump beam), $t_0$ is the emergence time of the wave at the surface, $T_{laser} = 12.554$ ns is the repetition time, $n$ is an integer which takes into account the successive generation of echoes due to the laser repetition rate and $\tau$ corresponds to the time at which the pump-probe coincidence would occur in the absence of mercury. We will name this method in the following "temporal method."

To evaluate $v$, we assign a first guess value to the integer $n$ and we thus derive $\Delta t$ from the measured $t_0$ and $\tau$. We will explain in Subsection III B, how the validation of the $n$ value and the measurement of the thickness $e_0$ can be done using the "imagery method" described below. Concerning $\tau$, we have previously measured it with an aluminum thin film, outside and inside the DAC (the variation of the optical path due to the presence of diamonds, around 2 mm thick each one, is negligible). For the present set-up, we obtained $\tau = 0.330 \pm 0.002$ ns.

Whereas this configuration allows a simple and quick way to extract the sound velocity,[34] its major and evident disadvantage comes from the need to know the gasket thickness at each thermodynamic condition. We thus have developed an additional set-up, called "imagery" method, which is able to determine both $v$ and $e_0$.

## B. Imagery method

A spherical wavefront is produced by the focused laser beam as described in Fig. 3. This wavefront travels through the sample, reaches its opposite surface and produces circular patterns. It can be demonstrated that the detection occurs in the far-field region which simplifies the analysis of the detection pattern.[35] The transition between the near-field and the far field occurs at the depth[36] $z_t \approx \frac{d^2}{4\lambda_{ac}}$ where d = 3 $\mu$m is the diameter of the laser spot and $\lambda_{ac}$ is the main wavelength of the acoustic wave packet. The peak frequency of the wave packet extracted from a Fourier transform of a temporal scan is roughly 0.6 GHz (see inset of Figure 2(a)) leading to $\lambda_{ac} \approx 1\,\mu$m. The transition distance $z_t = 2\,\mu$m is thus much smaller than the sample thickness and the detection is done in the far field.

A typical 100 $\times$ 100 $\mu$m image associated with the intensity profile is shown in Fig. 4. The center of the acoustics rings is spatially determined with an uncertainty smaller than $\pm 0.5\,\mu$m in the two directions perpendicular to the beam. Due to the repetition rate of the laser, these patterns are renewed
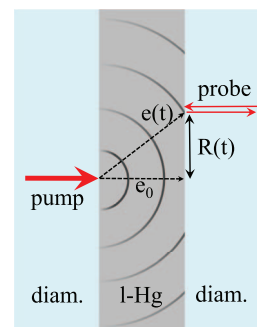


FIG. 3. Schematic diagram of the wavefronts in liquid mercury inside the DAC (note that diam. stands for diamond anvil). Spherical wavefronts produced by the focused pump beam are due to acoustic diffraction. On the probe side, the radius $R(t)$ of the circles appearing on the surface depends on the sample thickness $e_0$ and on the distance $e(t)$ between the probe and the source.
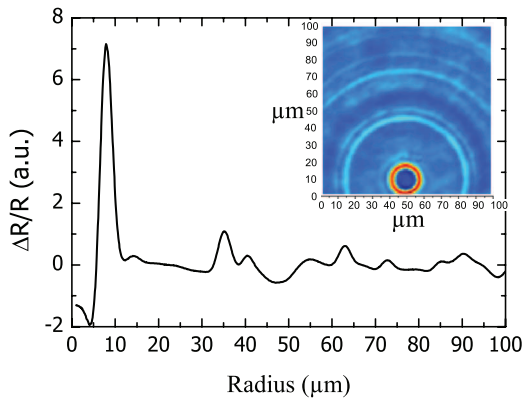
FIG. 4. Experimental image of the acoustic wavefront on the surface of liquid Hg at 1 GPa and 303 K for a pump-probe delay of t = 5.3 ns, with an arbitrary color scale (inset) and corresponding reflectivity of liquid mercury as a function of the radius (main figure).

every $T_{laser} = 12.554$ ns. Perfect circular rings are expected in the liquid phase (assuming that diamond culets stay parallels and are not deformed at high pressure[37]). The transition to a solid phase of mercury ($\alpha$-Hg) is easily detected since the acoustic pattern is then distorted due to crystal anisotropy.

For each thermodynamic condition, the acoustic wave front image is recorded as a function of the pump-probe delay, with a time step of 0.1 ns. All the corresponding integrated profiles can be stacked together into a graph (Fig. 5) where the color scale indicates the regions of high (red) and low (blue) reflectivity. The experimental temporal range is limited by the delay line but, to improve the visualization, the time scale of this graph is extended by repetition of the picture each $T_{laser}$. The main longitudinal waves propagating in mercury appear at 5, 17.5, and 30 ns corresponding to the pump repetition rate. The other ripples appearing in Fig. 5 correspond to the reflections of the main bulk wave and surface skimming bulk waves (SSBW). More details on these waves and the proce-
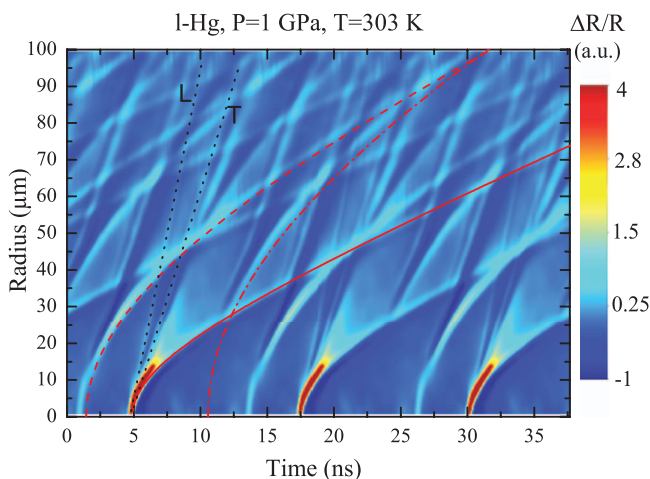


FIG. 5. Integrated profiles as a function of time at 1 GPa and 303 K. The time scale is extended by repetition of the picture each $T_{laser}$. The ripples in this picture evidence the growing of circular wavefronts on the surface of the sample. This picture shows the principal wavefront, here fitted with Eq. (A1) (red line), first and second reflections calculated as discussed in Appendix A (dashed and dotted-dashed red lines, respectively), and longitudinal and transverse SSBW in diamond (dotted black lines).
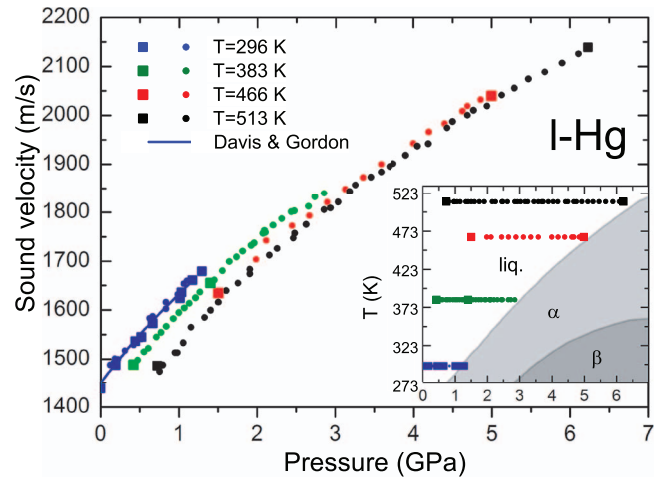


FIG. 6. Adiabatic sound velocity in liquid mercury as a function of pressure at various temperatures. (Squares) Imagery method. (Circles) Temporal method. The blue line is from Davis.[12] (Inset) Measurement points reported on the phase diagram of Hg.[31]

dure to extract both the velocity $v$ and the thickness $e_0$ from the imagery method are detailed in Appendix A.

## C. Results

We would like to emphasize that, while this imaging configuration is very powerful (both thickness and sound velocity of the sample are determined using a self-consistent method), it has the main disadvantage of being very time consuming. Therefore, we used the imagery method only at a few pressures along a given isotherm in order to measure both $v$ and $e_0$.

The velocities obtained by the imagery method are shown in Fig. 6. During one pressure downstroke, the experimental relative variation of the thickness is measured to be about 5%. Despite the increase of the sample chamber volume during the downstroke, the thickness remains nearly constant, as previously published.[38] This behavior is due to a plastic process inside the gasket.[39] A simple linear interpolation of these experimental points is used and provides a reliable estimate of the thickness variation as a function of pressure for the whole pressure and temperature range of the experiments. The sample thickness being known, the sound velocity can be directly extracted by a scan with temporal method. Figure 6 summarizes our complete results. The experimental data set is reported in Table I. The velocities obtained at ambient temperature agree with the data from Davis[12] up to 1.2 GPa.

## IV. EQUATION OF STATE

### A. Thermodynamic relations

The density variation as a function of pressure and temperature can be extracted from the sound velocity measurements via classical thermodynamic relations.[12,24,25] The adiabatic sound velocity[40,60] $v$ is related to the adiabatic compressibility by $\beta_S = 1/\rho v^2$ and to the thermal compressibility

TABLE I. Experimental sound velocities in liquid Hg.

| T = 296 K | | T = 383 K | | T = 466 K | | T = 513 K | |
|---|---|---|---|---|---|---|---|
| P (GPa) | v (m/s) | P (GPa) | v (m/s) | P (GPa) | v (m/s) | P (GPa) | v (m/s) |
| 0.00[a] | 1440 | 0.42[a] | 1490 | 1.50[a] | 1630 | 0.72[a] | 1490 |
| 0.00 | 1440 | 0.44 | 1490 | 1.51 | 1630 | 0.75 | 1470 |
| 0.12 | 1490 | 0.47 | 1500 | 1.51 | 1640 | 0.75 | 1470 |
| 0.18 | 1500 | 0.55 | 1510 | 1.98 | 1700 | 0.79 | 1490 |
| 0.19[a] | 1490 | 0.61 | 1520 | 2.11 | 1740 | 0.95 | 1510 |
| 0.22 | 1500 | 0.71 | 1540 | 2.44 | 1770 | 0.97 | 1510 |
| 0.31 | 1520 | 0.77 | 1550 | 2.66 | 1790 | 1.05 | 1530 |
| 0.42 | 1530 | 0.84 | 1570 | 2.89 | 1820 | 1.15 | 1560 |
| 0.44[a] | 1540 | 0.93 | 1580 | 3.12 | 1850 | 1.33 | 1580 |
| 0.52 | 1540 | 1.00 | 1590 | 3.35 | 1870 | 1.40 | 1600 |
| 0.52[a] | 1540 | 1.06 | 1600 | 3.58 | 1900 | 1.50 | 1620 |
| 0.62 | 1580 | 1.13 | 1610 | 4.00 | 1940 | 1.60 | 1640 |
| 0.66 | 1590 | 1.21 | 1620 | 4.20 | 1970 | 1.75 | 1650 |
| 0.66[a] | 1570 | 1.27 | 1640 | 4.40 | 1980 | 1.90 | 1670 |
| 0.66 | 1580 | 1.39 | 1660 | 4.63 | 2010 | 1.90 | 1680 |
| 0.83 | 1600 | 1.40 | 1660 | 4.69 | 2020 | 2.15 | 1710 |
| 0.83 | 1620 | 1.40[a] | 1660 | 4.86 | 2030 | 2.25 | 1730 |
| 0.98 | 1630 | 1.45 | 1660 | 5.00[a] | 2040 | 2.46 | 1750 |
| 1.01[a] | 1620 | 1.55 | 1680 | ... | ... | 2.48 | 1760 |
| 1.03[a] | 1640 | 1.64 | 1700 | ... | ... | 2.62 | 1780 |
| 1.06 | 1650 | 1.73 | 1710 | ... | ... | 2.85 | 1810 |
| 1.10 | 1660 | 1.81 | 1720 | ... | ... | 2.93 | 1810 |
| 1.17 | 1660 | 1.92 | 1730 | ... | ... | 3.03 | 1820 |
| 1.17[a] | 1660 | 1.96 | 1740 | ... | ... | 3.17 | 1840 |
| ... | ... | 2.07 | 1760 | ... | ... | 3.25 | 1860 |
| ... | ... | 2.09 | 1760 | ... | ... | 3.45 | 1870 |
| ... | ... | 2.10 | 1760 | ... | ... | 3.58 | 1880 |
| ... | ... | 2.20 | 1770 | ... | ... | 3.69 | 1900 |
| ... | ... | 2.31 | 1790 | ... | ... | 3.74 | 1900 |
| ... | ... | 2.43 | 1800 | ... | ... | 3.90 | 1920 |
| ... | ... | 2.47 | 1800 | ... | ... | 4.05 | 1940 |
| ... | ... | 2.65 | 1810 | ... | ... | 4.19 | 1940 |
| ... | ... | 2.73 | 1830 | ... | ... | 4.43 | 1970 |
| ... | ... | 2.85 | 1840 | ... | ... | 4.50 | 1990 |
| ... | ... | ... | ... | ... | ... | 4.69 | 2000 |
| ... | ... | ... | ... | ... | ... | 4.77 | 2010 |
| ... | ... | ... | ... | ... | ... | 4.94 | 2020 |
| ... | ... | ... | ... | ... | ... | 5.13 | 2040 |
| ... | ... | ... | ... | ... | ... | 5.29 | 2060 |
| ... | ... | ... | ... | ... | ... | 5.47 | 2070 |
| ... | ... | ... | ... | ... | ... | 5.68 | 2090 |
| ... | ... | ... | ... | ... | ... | 5.90 | 2110 |
| ... | ... | ... | ... | ... | ... | 6.11 | 2130 |
| ... | ... | ... | ... | ... | ... | 6.23 | 2140 |
| ... | ... | ... | ... | ... | ... | 6.23[a] | 2140 |

[a]These values are obtained by the imagery method (see Sec. IV B), the other ones are obtained by the temporal method (see Sec. IV A).

$\beta_T = 1/\rho(\partial\rho/\partial P)_T$ by

$$\beta_T = \beta_S + \frac{T\alpha_P^2}{\rho C_P}, \qquad (2)$$

where $C_P$ is the isobaric heat capacity per unit mass and $\alpha_P$ is the thermal expansion coefficient at constant pressure defined by

$$\alpha_P = \frac{1}{\rho}\left(\frac{\partial\rho}{\partial T}\right)_P. \qquad (3)$$

Equation (2) can be rewritten as

$$\left(\frac{\partial\rho}{\partial P}\right)_T = \frac{1}{v^2} + \frac{T\alpha_P^2}{C_P}. \qquad (4)$$

The integration of Eq. (4) between arbitrary pressures $P_1$ and $P_2$ at constant temperature leads to the equation

$$\rho(P_2, T) - \rho(P_1, T) = \int_{P_1}^{P_2} \frac{dP}{v^2(P,T)} + T\int_{P_1}^{P_2} \frac{\alpha_P^2(P,T)}{C_P(P,T)}dP, \qquad (5)$$

where the variation of $C_P$ with pressure can be evaluated via[41]

$$\left(\frac{\partial C_P}{\partial P}\right)_T = -\frac{T}{\rho}\left\{\left(\frac{\partial\alpha_P}{\partial T}\right)_P + \alpha_P^2\right\}. \qquad (6)$$

The three equations (3), (5), and (6) are used into a recursive procedure adapted from Ref. 24 described in Appendix B in order to obtain the density as a function of pressure and temperature.

## B. Results

In Figs. 7 and 8, we show, respectively, $\rho$ and $\alpha_P$ as a function of pressure as derived from our data. Other derived quantities are the isothermal bulk modulus $B_T = \beta_T^{-1}$ and the first derivative of the bulk modulus $B_T' = (\partial B_T/\partial P)_T$. They are shown in Figs. 9(a) and 9(b), respectively.

The uncertainties have been evaluated by the introduction of small perturbations in the three input quantities $v(P,T)$, $\rho(P_0, T)$, and $C_P(P_0, T)$. An increase or decrease of the sound velocity data by 10 m/s (0.75%) leads to a variation of $\pm 0.15\%$ of the density, $\pm 1.7\%$ of the thermal expansion, and $\pm 0.7\%$ of the heat capacity. The relative uncertainty in $\rho(P_0)$[42] is roughly $10^{-4}\%$ which produces relative variations of $\pm 0.5\%$ for the $\alpha_P$ and of $\pm 0.8\%$ for the $C_P$. According to Douglas,[43] the heat capacity $C_P(P_0, T)$ is known at $\pm 0.3\%$. This leads to relative variations of $\pm 0.5\%$ for the $\alpha_P$ and of $\pm 0.8\%$ for the final $C_P$. Finally, the different uncertainties are quadratically summed. The maximal uncertainties associated with the absolute measurements of the different quantities are
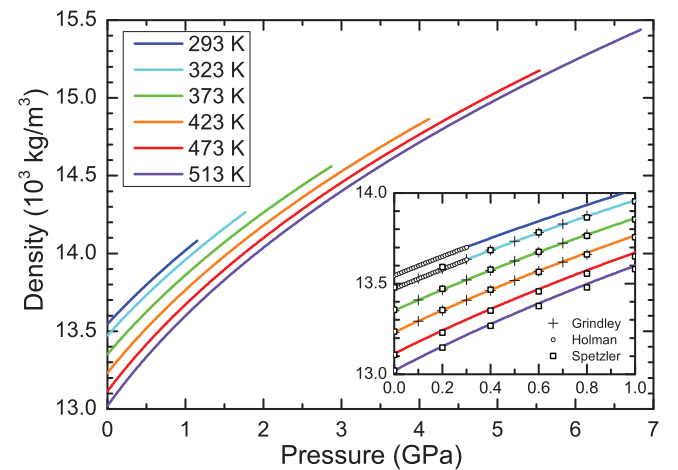


FIG. 7. Density of liquid Hg versus pressure at different temperatures. The calculation procedure from sound velocity measurements is explained in the text. (Inset) Comparison between our work and the data from Holman,[42] Grindley,[62] and Spetzler.[13]
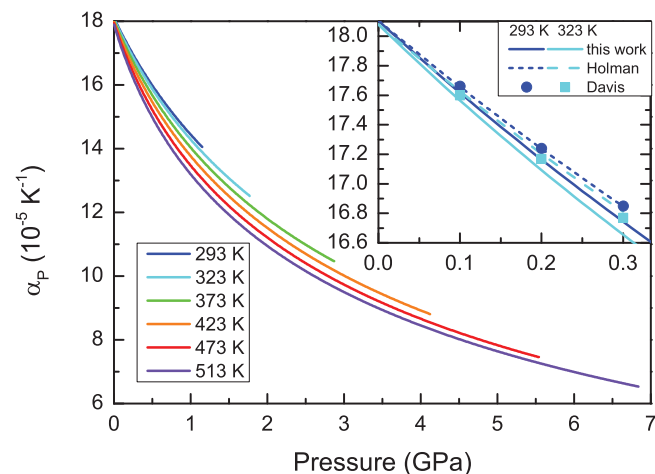
FIG. 8. Coefficient of thermal expansion $\alpha_P$ of liquid Hg as a function of pressure at different temperatures. (Inset) Comparison with the data of Davis[12] and Holman.[42]

around $\pm 0.15\%$ for the density, $\pm 3.8\%$ for the thermal expansion, and $\pm 3.4\%$ for the heat capacity. Table II summarizes all the thermodynamic properties obtained by this procedure.

## C. Equations of state

Analytical EOS are widely used for solids in order to extrapolate density measurements at P and T values unreached experimentally, and they are usually based on some hypotheses on the P and T variation of one of the known thermodynamic coefficients. It is unclear that such hypotheses remain valid in the liquid state where density variations with P and T are by far larger than in the solid.

It is nevertheless currently assumed that EOS derived for the solid state can also be applied to the liquid state of metals due to the relatively small compressibility change on melting.[44] The availability here of new experimentally derived values for the bulk modulus of liquid mercury in a wide range of pressure enables us to test the validity of this assumption.
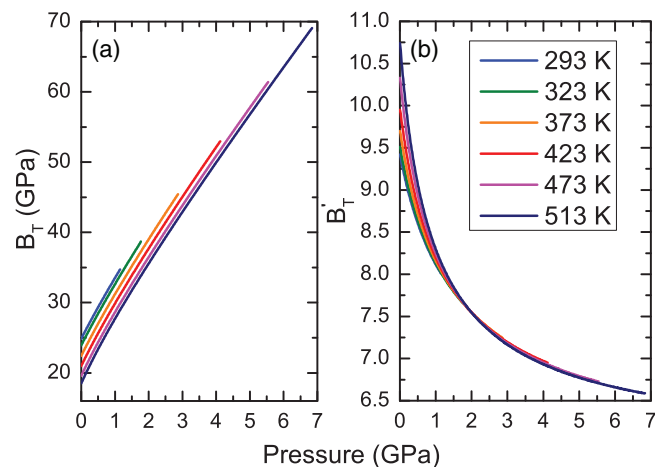


FIG. 9. (a) Isothermal bulk modulus $B_T$ as a function of pressure at different temperatures. (b) First derivative of the isothermal bulk modulus $B_T'$ as a function of pressure at different temperatures.

Use of Taylor series expansion is one of the easiest approaches to develop a P-V equation. A series expansion of P in $\Delta V / V$ truncated at the second order generates what is known as the Davis Gordon approximation (see Eq. (15) in Ref. 12), which is largely used for solid samples. An empirical EOS which was, conversely, developed for liquids, in particular for water, is the Tait equation[45] which express V as a function of P using two empirical parameters which are function of the temperature but pressure independent. However, these two parameters do not have particular physical meanings.

An alternative approach consists in formulating some hypotheses on the pressure dependence of the bulk modulus. The most simple approximation is the Murnaghan equation[46] where the bulk modulus $B$ is considered to vary linearly with pressure ($B = B_0 + B_0' P$ where $B_0 = B_T(P_0)$ and $B_0' = B_T'(P_0)$), while the widely used Birch-Murnaghan EOS[47] consists in a series expansion of the free energy in terms of volume. The Kumari-Dass EOS[48] assumes that the ratio of the second to the first pressure derivative of the bulk modulus, $B_0'' / B_0'$, is a parameter independent of pressure. This equation was applied successfully to some simple liquid metals such as alkali metals.[49]

Following the work of Stacey,[50] Vinet *et al.*[51] proposed an equation based on a potential with a soft repulsive contribution. This equation, proposed originally for the solids, was applied to liquid alkali metals[52] up to 2 GPa but with the assumption that at high pressure all materials are expected to convert to a Thomas-Fermi state. Also, Holzapfel[53] proposed a modified version of the Vinet EOS.

In order to test the validity of those different equations, we calculated the pressure dependence of the density at 513 K as predicted by each of them, using the same, experimentally derived, parameters ($B_0 = 18.5$ GPa, $B_0' = 10.7$, $B_0'' = -5.1$ GPa$^{-1}$, and $\rho_0 = 13019.8$ kg/m$^3$). A comparison with our experimental results is reported in Fig. 10.

As readily seen on this figure, the Kumari-Dass and the Murnaghan EOS badly reproduce our results, as strong deviations are observed in the present pressure range. Similar discrepancies are observed with the Vinet and Holzapfel EOS.

Finally, one can observe that the Birch-Murnaghan equation and the Taylor series expansion proposed by Davis and Gordon can be considered as good analytical EOS for liquid Hg, even at high density.

## V. DISCUSSION

In Fig. 11, we report present and previous[5] measurements of the adiabatic sound velocity as a function of density for different temperatures. The density ranges from the low density non-metallic state to the high-density metallic one.[5]

As previously observed by Kohno and co-workers,[5] in the NM region ($\rho < 9 \times 10^3$ kg/m$^3$), $v$ varies slowly with density and its temperature (and pressure) dependence is of the same order of magnitude as the density one. The situation is opposite on the metallic (M) side ($\rho > 9 \times 10^3$ kg/m$^3$).

As shown in Fig. 11, the sound velocity can be described as a unique functional of density in the overall density range, pressure, and temperature variations producing only second

TABLE II. Various thermodynamical properties of liquid Hg up to 513 K and 7 GPa. The uncertainties are discussed in the text.

| T (K) | P (GPa) | $\rho$ (kg/m³) | $\alpha_P$ ($10^{-4}$ K$^{-1}$) | $\beta_S$ ($10^{-2}$ GPa$^{-1}$) | $B_S$ (GPa) | $\beta_T$ ($10^{-2}$ GPa$^{-1}$) | $B_T$ (GPa) |
|---|---|---|---|---|---|---|---|
| 293 | 0.0 | 13545.8 | 1.81 | 3.51 | 28.5 | 4.02 | 24.9 |
| 293 | 0.2 | 13650 | 1.72 | 3.29 | 30.4 | 3.75 | 26.7 |
| 293 | 0.4 | 13750 | 1.64 | 3.10 | 32.2 | 3.51 | 28.5 |
| 293 | 0.8 | 13930 | 1.50 | 2.80 | 35.8 | 3.14 | 31.9 |
| 293 | 1.0 | 14020 | 1.44 | 2.67 | 37.4 | 2.98 | 33.5 |
| 323 | 0.0 | 13472.5 | 1.81 | 3.61 | 27.7 | 4.18 | 23.9 |
| 323 | 0.2 | 13580 | 1.71 | 3.38 | 29.6 | 3.88 | 25.8 |
| 323 | 0.4 | 13680 | 1.63 | 3.18 | 31.5 | 3.63 | 27.6 |
| 323 | 0.8 | 13870 | 1.49 | 2.86 | 35.0 | 3.23 | 31.0 |
| 323 | 1.0 | 13960 | 1.43 | 2.72 | 36.7 | 3.07 | 32.6 |
| 323 | 1.6 | 14200 | 1.29 | 2.41 | 41.6 | 2.68 | 37.4 |
| 373 | 0.0 | 13351.4 | 1.80 | 3.80 | 26.3 | 4.46 | 22.4 |
| 373 | 0.2 | 13470 | 1.70 | 3.53 | 28.3 | 4.11 | 24.3 |
| 373 | 0.4 | 13570 | 1.61 | 3.31 | 30.2 | 3.83 | 26.1 |
| 373 | 0.8 | 13770 | 1.46 | 2.96 | 33.8 | 3.38 | 29.6 |
| 373 | 1.0 | 13860 | 1.40 | 2.82 | 35.5 | 3.20 | 31.2 |
| 373 | 1.6 | 14110 | 1.26 | 2.48 | 40.4 | 2.78 | 36.0 |
| 373 | 1.8 | 14190 | 1.22 | 2.38 | 41.9 | 2.67 | 37.5 |
| 373 | 2.0 | 14260 | 1.18 | 2.30 | 43.5 | 2.56 | 39.0 |
| 373 | 2.2 | 14330 | 1.15 | 2.22 | 45.0 | 2.47 | 40.5 |
| 373 | 2.6 | 14470 | 1.08 | 2.08 | 48.0 | 2.30 | 43.5 |
| 423 | 0.0 | 13231.7 | 1.80 | 4.01 | 25.0 | 4.77 | 21.0 |
| 423 | 0.2 | 13350 | 1.68 | 3.71 | 27.0 | 4.36 | 22.9 |
| 423 | 0.4 | 13470 | 1.59 | 3.46 | 28.9 | 4.04 | 24.7 |
| 423 | 0.8 | 13670 | 1.44 | 3.08 | 32.5 | 3.54 | 28.2 |
| 423 | 1.0 | 13770 | 1.38 | 2.92 | 34.2 | 3.35 | 29.9 |
| 423 | 1.6 | 14020 | 1.23 | 2.55 | 39.1 | 2.89 | 34.7 |
| 423 | 1.8 | 14100 | 1.19 | 2.46 | 40.7 | 2.76 | 36.2 |
| 423 | 2.0 | 14180 | 1.15 | 2.37 | 42.3 | 2.65 | 37.7 |
| 423 | 2.2 | 14250 | 1.12 | 2.28 | 43.8 | 2.55 | 39.2 |
| 423 | 2.6 | 14390 | 1.06 | 2.14 | 46.8 | 2.37 | 42.2 |
| 423 | 3.0 | 14530 | 1.00 | 2.01 | 49.8 | 2.22 | 45.1 |
| 423 | 3.2 | 14590 | 0.98 | 1.95 | 51.2 | 2.15 | 46.5 |
| 423 | 3.4 | 14650 | 0.95 | 1.90 | 52.7 | 2.09 | 47.9 |
| 423 | 3.6 | 14710 | 0.93 | 1.85 | 54.1 | 2.03 | 49.3 |
| 423 | 4.0 | 14830 | 0.89 | 1.76 | 56.9 | 1.92 | 52.1 |
| 473 | 0.0 | 13113.4 | 1.79 | 4.25 | 23.5 | 5.11 | 19.6 |
| 473 | 0.2 | 13240 | 1.67 | 3.90 | 25.6 | 4.63 | 21.6 |
| 473 | 0.4 | 13360 | 1.57 | 3.63 | 27.6 | 4.26 | 23.5 |
| 473 | 0.8 | 13570 | 1.41 | 3.20 | 31.2 | 3.71 | 27.0 |
| 473 | 1.0 | 13670 | 1.35 | 3.03 | 33.0 | 3.49 | 28.6 |
| 473 | 1.6 | 13940 | 1.20 | 2.64 | 37.9 | 2.99 | 33.4 |
| 473 | 1.8 | 14020 | 1.16 | 2.53 | 39.5 | 2.86 | 35.0 |
| 473 | 2.0 | 14100 | 1.12 | 2.44 | 41.1 | 2.74 | 36.5 |
| 473 | 2.2 | 14180 | 1.09 | 2.35 | 42.6 | 2.63 | 38.0 |
| 473 | 2.6 | 14320 | 1.03 | 2.19 | 45.6 | 2.44 | 40.9 |
| 473 | 3.0 | 14460 | 0.97 | 2.06 | 48.5 | 2.28 | 43.8 |
| 473 | 3.2 | 14520 | 0.95 | 2.00 | 50.0 | 2.21 | 45.3 |
| 473 | 3.4 | 14580 | 0.93 | 1.94 | 51.4 | 2.14 | 46.7 |
| 473 | 3.6 | 14650 | 0.91 | 1.89 | 52.9 | 2.08 | 48.1 |
| 473 | 4.0 | 14760 | 0.87 | 1.80 | 55.7 | 1.97 | 50.9 |
| 473 | 4.2 | 14820 | 0.85 | 1.75 | 57.1 | 1.91 | 52.3 |
| 473 | 4.4 | 14880 | 0.83 | 1.71 | 58.5 | 1.86 | 53.7 |
| 473 | 5.0 | 15040 | 0.78 | 1.60 | 62.6 | 1.73 | 57.8 |
| 473 | 5.2 | 15090 | 0.77 | 1.56 | 64.0 | 1.69 | 59.1 |
| 473 | 5.4 | 15140 | 0.75 | 1.53 | 65.4 | 1.65 | 60.5 |
| 513 | 0.0 | 13019.8 | 1.79 | 4.48 | 22.3 | 5.41 | 18.5 |
| 513 | 0.2 | 13150 | 1.65 | 4.08 | 24.5 | 4.87 | 20.5 |
| 513 | 0.4 | 13280 | 1.54 | 3.77 | 26.5 | 4.45 | 22.5 |

TABLE II.  *(Continued).*

| T (K) | P (GPa) | $\rho$ (kg/m$^3$) | $\alpha_P$ ($10^{-4}$ K$^{-1}$) | $\beta_S$ ($10^{-2}$ GPa$^{-1}$) | $B_S$ (GPa) | $\beta_T$ ($10^{-2}$ GPa$^{-1}$) | $B_T$ (GPa) |
|---|---|---|---|---|---|---|---|
| 513 | 0.8 | 13500 | 1.38 | 3.31 | 30.2 | 3.84 | 26.0 |
| 513 | 1.0 | 13600 | 1.32 | 3.13 | 32.0 | 3.61 | 27.7 |
| 513 | 1.6 | 13870 | 1.17 | 2.71 | 36.9 | 3.08 | 32.5 |
| 513 | 1.8 | 13960 | 1.13 | 2.60 | 38.5 | 2.94 | 34.1 |
| 513 | 2.0 | 14040 | 1.09 | 2.50 | 40.1 | 2.81 | 35.6 |
| 513 | 2.2 | 14110 | 1.06 | 2.40 | 41.6 | 2.70 | 37.1 |
| 513 | 2.6 | 14260 | 1.00 | 2.24 | 44.6 | 2.50 | 40.0 |
| 513 | 3.0 | 14400 | 0.95 | 2.10 | 47.6 | 2.33 | 42.9 |
| 513 | 3.2 | 14470 | 0.93 | 2.04 | 49.0 | 2.26 | 44.3 |
| 513 | 3.4 | 14530 | 0.90 | 1.98 | 50.5 | 2.19 | 45.8 |
| 513 | 3.6 | 14590 | 0.88 | 1.93 | 51.9 | 2.12 | 47.2 |
| 513 | 4.0 | 14710 | 0.85 | 1.83 | 54.7 | 2.00 | 49.9 |
| 513 | 4.2 | 14770 | 0.83 | 1.78 | 56.1 | 1.95 | 51.3 |
| 513 | 4.4 | 14830 | 0.81 | 1.74 | 57.5 | 1.90 | 52.7 |
| 513 | 5.0 | 14990 | 0.76 | 1.62 | 61.7 | 1.76 | 56.8 |
| 513 | 5.2 | 15050 | 0.75 | 1.59 | 63.0 | 1.72 | 58.1 |
| 513 | 5.4 | 15100 | 0.74 | 1.55 | 64.4 | 1.68 | 59.5 |
| 513 | 6.0 | 15240 | 0.70 | 1.46 | 68.4 | 1.57 | 63.5 |
| 513 | 6.2 | 15290 | 0.69 | 1.43 | 69.8 | 1.54 | 64.8 |
| 513 | 6.4 | 15340 | 0.68 | 1.41 | 71.1 | 1.51 | 66.2 |
| 513 | 6.8 | 15430 | 0.66 | 1.36 | 73.8 | 1.45 | 68.8 |

order effects. In particular, its temperature dependence is small and becomes weaker and weaker with increasing density, as can be seen in the inset of Fig. 11. The observed density dependence can be described by the simple power law

$$v = v_0 \left( \frac{\rho}{\rho_0} \right)^{\alpha} \tag{7}$$

with $\alpha = 2.72 \pm 0.02$[54] (dotted line in Fig. 11). To our knowledge, this is the first time that the existence of a scaling law is probed on such a large range of density variation.

The existence of such a power law for the sound velocity in a metal may appear as natural. Indeed, such a law has been proposed, long ago, by Bohm and Staver[26] (dot-dashed line in Fig. 11). Nevertheless in the BS approximation, $\alpha$ has the much smaller value $\alpha = 1/3$, basically one order of magnitude smaller. Actually, the BS theory reasonably predicts the sound velocity in liquid metals in the solid like regime (THz) where relaxation effects are absent and the main mechanism governing the propagation of collective excitation is the electron screening.[55] Conversely, in the adiabatic regime, ionic
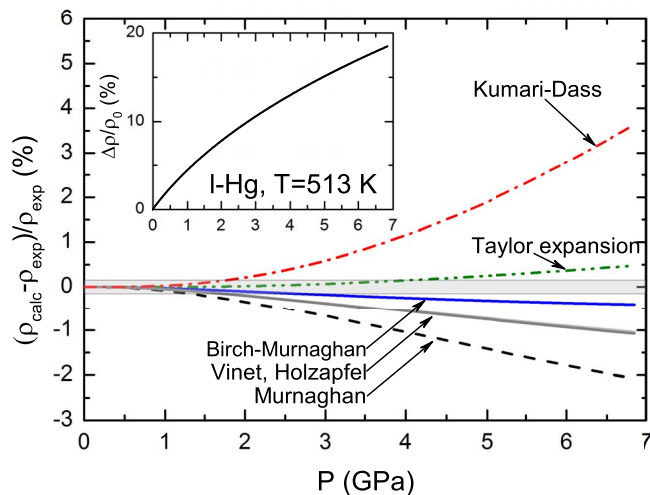


FIG. 10. Relative deviation between the experimental density and calculated density obtained by the predictions of many equations of state (no fit). Physical hypotheses concerning the EOS are discussed in the text. The gray region shows the uncertainty on the experimental determination of the density. (Inset) Relative variation of the experimental density which shows the accuracy of the various EOS.
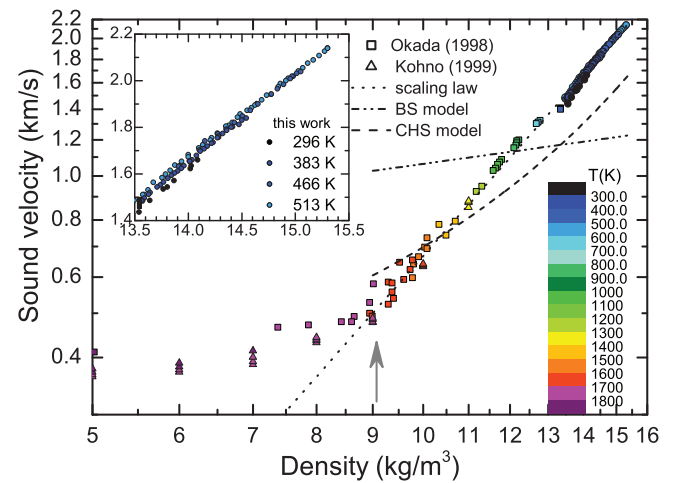


FIG. 11. Adiabatic sound velocity as a function of density at different temperatures in a log-log scale and linear scale (inset). Sound velocity data from this work (circles) are plot with experimental data from Kohno[5] (triangles up) and Okada[61] (squares). Gray arrow indicates the density at which M-NM transition occurs. The dotted line indicates a power law discussed in the text. The dot-dashed and dashed lines are calculated at 513 K from the BS[26] and Charged Hard-Sphere (CHS)[27] models, respectively.

size and ionic relaxation effects become predominant and the BS approximation gives rise to erroneous predictions.

An alternative approach is to consider a charged hard sphere model (CHS) for the liquid metal, where positively charged hard spheres interact through a Coulomb potential in a background of non-interacting conduction electrons. In such a model, ions diffusion is taken into account and the adiabatic sound velocity is directly derived from the compressibility of the system, which is itself a simple function of the packing fraction (Eqs. (7)–(9) of Ref. 27). Thus, modeling of the charged hard sphere radius $R$ as a function of P and T and of the functional dependence of compressibility on the packing fraction $\eta$ results in a simple expression for the sound velocity dependence on density. We calculated the prediction of the CHS model using $\eta$ as derived from simple hard sphere simulations, Ref. 56. As it can be seen in Fig. 11 (dashed line), this prediction correctly reproduces the variation of the sound velocity with density in the high density regime (i.e., for high packing fraction), even if the absolute value of the predicted velocity is a factor 1.3 lower than in the real liquid. However, the CHS model fails in reproducing the overall trend, as the hard sphere radius variation as a function of pressure and temperature is unknown and not correctly reproduced by the aforementioned simulations. This comparison again indicates that the repulsive part of the potential mainly determines the value and the density dependence of the adiabatic sound velocity in the high density regime. The availability of sound velocity data on a wide range of density in these high density conditions is thus fundamental to validate models for the repulsive part of the ion-ion effective potential.

In summary, we performed accurate measurements of the adiabatic sound velocity in liquid mercury up to 7 GPa and temperatures up to 520 K using an original experimental method, the picosecond acoustics surface imaging in DAC. We show that the thickness of the sample in a DAC can be accurately determined *in situ* by this technique as a function of pressure and temperature. Using the measured velocities data, the density of the fluid is derived together with other thermodynamic parameters.

Finally, we compared the measured sound velocity as a function of density with previously measured values in expanded mercury down to the M-NM transition.[5] We show that the adiabatic sound velocity can be described as a unique functional of density in the whole investigated metallic state, while temperature and/or pressure variations only produce second order effects. We show that simple models like the Bohm-Staver model or the charge hard sphere model, usually employed to predict sound velocities in the solid (or in the unrelaxed liquid[10]) and in the relaxed liquid, respectively, fail in reproducing the observed density trend. We thus believe that these new sound velocities data can be used to validate current models of the ion-ion repulsive potential in liquid mercury.

From a more general point of view, our study demonstrates that picosecond acoustics in DAC is a powerful technique to quantitatively extract the sound velocities, the density or other thermodynamical quantities in liquid metals under extreme conditions. These state-of-the-art experiments will certainly be useful in several applied problems and many other fields such as geophysics.

## APPENDIX A: ANALYZING RIPPLES FROM SURFACE IMAGING

Let us consider the evolution of spherical wavefronts inside the sample as shown in Fig. 3. The time evolution of the ring diameters $R(t)$ appearing at the surface is given by

$$R(t) = \sqrt{e^2(t) - e_0^2}, \qquad (A1)$$

where $e(t) = v(t + nT_{laser} - \tau)$ is the distance covered by the acoustics wave propagating inside the sample, $v$ is the sound velocity, and $e_0$ is the sample thickness. The parameters $n$ and $\tau$ are the same as in Eq. (1). Equation (A1) is fitted to the ripple (as shown in Fig. 5) with the sound velocity $v$ and the arrival time $t_0$ as free parameters. Then the thickness $e_0$ is deduced with Eq. (1).

Knowing $v$ and $e_0$, it is now straightforward to predict the radius evolution $R_i(t)$ for the $i$th reflected wave

$$R_i(t) = v\sqrt{e_i(t)^2 - [(2i + 1)e_0]^2}. \qquad (A2)$$

Equation (A2) can be also written as

$$R_i(t) = v\sqrt{(t + n_i T_{laser} - \tau)^2 - (t_0^i + n_i T_{laser} - \tau)^2}, \qquad (A3)$$

where $t_0^i$ is the emergence time of this reflected wave on the pump beam propagation axis and $n_i$ is an integer given by the relation

$$n_i = (2i + 1)n + \frac{(2i + 1)(t_0 - \tau) - (t_0^i - \tau)}{T}. \qquad (A4)$$

Pink and green lines shown in Fig. 5 stand for the first $(i = 1)$ and the second $(i = 2)$ reflections, respectively. The good agreement between the ripples and the lines is obtained without fit.

An accurate determination of the experimental radius $R$ requires a correct interpretation of the integrated profile which, otherwise, could lead to systematic errors on the parameters $t_0$ and $v$. The detected echo has an antisymmetric shape (as observed in Fig. 4 between 0 and 10 $\mu$m) which is related to the bipolar strain of the acoustic pulse. This bipolar strain can be explained by the generation, propagation, and detection process involving the acoustic pulse.[19,35] The thermoelastic generation of the pulse in the liquid Hg in contact with the diamond produces an unipolar and asymmetric strain profile.[19] Just after the generation, the acoustic pulse is immediately reflected at the diamond/mercury interface. As a consequence, the spatial extension of the pulse is doubled and the shape becomes unipolar.[19] During its propagation from the near field to the far field, the acoustic pulse transforms from a unipolar to a bipolar shape[35] which explains the antisymmetric shape of the detected echo.[19] We deduce that the experimental value $R$ of the radius corresponds to the midpoint

of the perturbation seen in surface. This conclusion remains correct for large values of $R$ because the deformation of the detected echo due to the acoustic dispersion or attenuation is supposed negligible.[19]

As evident on Fig. 5, some ripples have a radius with a linear time dependence. This is the signature of surface skimming bulk waves (SSBW) propagating in the diamond anvil, parallel to the surface. These waves arise at the critical angle of the Snell-Descartes law of acoustic refraction at the diamond-mercury interface. Above this critical angle the reflection is total and any other SSBW cannot be generated. This angle is estimated to be $4.3°$ between the propagating wave vector in the mercury and the diamond surface. In interferometry, two kinds of SSBW are visible with mean velocities $c_L = 18 \pm 1$ km/s and $c_T = 12 \pm 1$ km/s corresponding to the longitudinal and transverse velocities in the diamond, as expected.

## APPENDIX B: RECURSIVE NUMERICAL PROCEDURE

We present in this Appendix, the procedure used to compute the density from the sound velocity measurements. This procedure needs as input parameters the sound velocity as a function of temperature and pressure, and the temperature variations of $\rho$ and $C_P$ at room pressure $P_0$. All high pressure sound velocity values come from our work (see Table I and Fig. 6). At ambient pressure, the data from Coppens *et al.*[57] and Jarzynski,[58] $v(P_0, T)$, are appended to our experimental values. All data are interpolated and smoothed by a polynomial function $P = \sum_{i,j} a_{ij}(T - 273.15)^i v^j$. The function $P(T, v)$ is chosen because it gives a better fit than $v(P, T)$ for the same number of parameters. The coefficients $a_{ij}$ are shown in Table III.

The density $\rho(P_0, T)$ is calculated from the polynomial formula given by Holman (Eq. (28) in Ref. 42). The coefficient of thermal expansion $\alpha_P(P_0, T)$ is directly deduced from the density using Eq. (3). The values of the heat capacity $C_P(P_0, T)$ between 273 K and 800 K are interpolated from the measured values of Ref. 43 using a third order polynomial function. The best interpolation relation obtained is $C_P(P_0, T) = 152.77 - 0.0659T + 6.90 \times 10^{-5}T^2 - 1.30 \times 10^{-8}T^3$ with T in K and $C_P$ in J kg$^{-1}$K$^{-1}$.

Starting from the room pressure $P_0$, the values at higher pressures are obtained by a series of small pressure increments, $\Delta P = P_2 - P_1 = 0.01$ GPa, from the already determined pressure point $P_1$ to the next calculated pressure point $P_2$. At each pressure step, the quantities $\rho$, $\alpha_P$, and $C_P$ are calculated. All the quantities are evaluated at each temperature between 293 K and 513 K with a temperature step

$\Delta T = 1$ K. The basis of the calculation is Eq. (5). The first integral in Eq. (5) is evaluated numerically with the function $P(T, v)$. This term represents the major contribution to the variation of the density; it depends only on the velocity and on an accurate numerical integration. The second term of Eq. (5) contributes for roughly 15% of the density change and is evaluated iteratively until convergence. In the first step of the iterative process, the quantity $T\alpha_P^2/C_P$ is kept constant, leading to a first crude approximation of the density at pressure $P_2$. Then $\alpha(P_2, T)$ is deduced from this first approximation using Eq. (3). In the second iterative step, the variation of $\alpha_P$ is taken into account by a linear interpolation between $\alpha_P(P_1, T)$ and $\alpha_P(P_2, T)$ and introduced in Eq. (5), while $C_P$ is still kept constant leading to a first refinement of the density value. Keeping $C_P$ constant during that integration step is a valid approximation because the relative variation of $C_P$ with $P$ is negligible compared to that of $\alpha_P$. This process is repeated until the convergence of $\rho(P_2, T)$ value. During this procedure, $\alpha_P(P_2, T)$ is smoothed by a third order polynomial to avoid the side effects occurring with the numerical derivation. Finally, $C_P(P_2, T)$ at the new pressure $P_2$ is obtained by a linear extrapolation of the $C_P(P_1, T)$ value at $P_1$ and its derivative through Eq. (6). The consistency of the method is checked by verifying that the thermodynamic relation $(\frac{\partial \alpha_P}{\partial T})_P = (\frac{\partial \beta_T}{\partial P})_T$ is satisfied with a relative accuracy better than 1% in the whole P and T range.

In order to evaluate the robustness of this numerical procedure, we have performed a test on the well-known thermodynamic data of liquid water[59] in the temperature range 280–340 K and the pressure range 0.1–50 MPa with $\Delta T = 1$ K and $\Delta P =$0.1 MPa. We have obtained results in very good agreement with the literature data, the comparison providing the relative uncertainties due to the numerical procedure. The uncertainties are $\pm0.002$% for the density, $\pm1$% for the thermal expansion and $\pm0.5$% for the heat capacity.

TABLE III. $a_{ij}$ coefficients for $P = \sum_{i,j} a_{ij}(T - 273.15)^i v^j$ with $P$ in GPa, T in K and $v$ in m/s.

| i/j | 0 | 1 | 2 |
|---|---|---|---|
| 0 | 4.00423 | $-1.006 \times 10^{-2}$ | $5.01139 \times 10^{-6}$ |
| 1 | $5.81263 \times 10^{-4}$ | $1.23466 \times 10^{-6}$ | ... |
| 2 | $8.17121 \times 10^{-7}$ | ... | ... |

[1] T. S. Ingebrigtsen, T. B. Schröder, and J. C. Dyre, Phys. Rev. X **2**, 011011 (2012).
[2] L. J. Norrby, J. Chem. Educ. **68**, 110 (1991).
[3] F. Calvo, E. Pahl, M. Wormit, and P. Schwerdtfeger, Angew. Chem. Int. Ed. **52**, 7583 (2013).
[4] W. Jank and J. Hafner, Phys. Rev. B **42**, 6926 (1990).
[5] H. Kohno and M. Yao, J. Phys.: Condens. Matter **11**, 5399 (1999).
[6] P. Edwards, T. Ramakrishnan, and C. Rao, J. Phys. Chem. **99**, 5228 (1995).
[7] K. Suzuki, M. Inatake, S. Fujiwaka, M. Yao, and H. Endo, J. Phys. Colloq. **41**, C8-66 (1980).
[8] S. Munejiri, F. Shimojo, and K. Hoshino, J. Phys.: Condens. Matter **10**, 4963 (1998).
[9] N. Ashcroft and N. Mermin, *Solid State Physics, Science: Physics* (Saunders College, 1976).
[10] L. E. Bove, F. Sacchetti, C. Petrillo, B. Dorner, F. Formisano, and F. Barocchi, Phys. Rev. Lett. **87**, 215504 (2001).
[11] L. Sani, L. Bove, C. Petrillo, and F. Sacchetti, in *Proceedings of the 12th International Conference on Liquid and Amorphous Metals, 2007* [J. Non-Crystal. Solids **353**, 3139 (2007)].
[12] L. A. Davis and R. B. Gordon, J. Chem. Phys. **46**, 2650 (1967).
[13] H. Spetzler, M. Meyer, and C. Tin, High Temp.-High Press. **7**, 481 (1975).
[14] J. R. MacDonald, Rev. Mod. Phys. **41**, 316 (1969).
[15] S. Jiu-Xun, W. Fu-Qian, W. Qiang, and C. Ling-Cang, Appl. Phys. Lett. **89**, 121922 (2006).
[16] C. Thomsen, H. T. Grahn, H. J. Maris, and J. Tauc, Phys. Rev. B **34**, 4129 (1986).
[17] F. Decremps, L. Belliard, B. Perrin, and M. Gauthier, Phys. Rev. Lett. **100**, 035502 (2008).

[18]N. Chigarev, P. Zinin, L.-C. Ming, G. Amulele, A. Bulou, and V. Gusev, Appl. Phys. Lett. **93**, 181905 (2008).

[19]O. B. Wright, B. Perrin, O. Matsuda, and V. E. Gusev, Phys. Rev. B **78**, 024303 (2008).

[20]F. Decremps, L. Belliard, B. Couzinet, S. Vincent, P. Munsch, G. Le Marchand, and B. Perrin, Rev. Sci. Instrum. **80**, 073902 (2009).

[21]Y. Sugawara, O. B. Wright, O. Matsuda, M. Takigahira, Y. Tanaka, S. Tamura, and V. E. Gusev, Phys. Rev. Lett. **88**, 185504 (2002).

[22]F. Decremps, L. Belliard, M. Gauthier, and B. Perrin, Phys. Rev. B **82**, 104119 (2010).

[23]S. Zhang, E. Peronne, L. Belliard, S. Vincent, and B. Perrin, J. Appl. Phys. **109**, 033507 (2011).

[24]J. Daridon, B. Lagourette, and J.-P. Grolier, Int. J. Thermophys. **19**, 145 (1998).

[25]M. J. Dávila and J. M. Trusler, J. Chem. Thermodyn. **41**, 35 (2009).

[26]D. Bohm and T. Staver, Phys. Rev. **84**, 836 (1951).

[27]Y. Rosenfeld, J. Phys. Condens. Matter **11**, L71 (1999).

[28]J.-Y. Duquesne and B. Perrin, Phys. Rev. B **68**, 134205 (2003).

[29]B. Perrin, C. Rossignol, B. Bonello, and J.-C. Jeannet, Physica B **263–264**, 571 (1999).

[30]F. Datchi, R. LeToullec, and P. Loubeyre, J. Appl. Phys. **81**, 3333 (1997).

[31]W. Klement, A. Jayaraman, and G. C. Kennedy, Phys. Rev. **131**, 1 (1963).

[32]C. Guminski, J. Phase Equilib. **23**, 184 (2002).

[33]C. Guminski, J. Phase Equilib. **14**, 219 (1993).

[34]In addition, the shift of the temporal echo allows to measure accurately the melting line for nontransparent materials.[20]

[35]N. C. R. Holme, B. C. Daly, M. T. Myaing, and T. B. Norris, Appl. Phys. Lett. **83**, 392 (2003).

[36]H.-N. Lin, R. Stoner, H. Maris, and J. Tauc, J. Appl. Phys. **69**, 3816 (1991).

[37]R. J. Hemley, H.-K. Mao, G. Shen, J. Badro, P. Gillet, M. Hanfland, and D. Husermann, Science **276**, 1242 (1997).

[38]A. Dewaele, J. H. Eggert, P. Loubeyre, and R. Le Toullec, Phys. Rev. B **67**, 094112 (2003).

[39]D. J. Dunstan, Rev. Sci. Instrum. **60**, 3789 (1989).

[40]The sound waves propagate adiabatically up to a frequency $f$ given by $f = v^2 \rho C_V / 2\pi\kappa$ where $\kappa$ is the thermal conductivity and $C_V$ is the isochoric specific heat.[60] In the liquid mercury $f \approx 100$ GHz well above the 10 GHz reached in our experiments.

[41]E. Wilhelm, J. Solution Chem. **39**, 1777 (2010).

[42]G. J. F. Holman and C. A. ten Seldam, J. Phys. Chem. Ref. Data **23**, 807 (1994).

[43]T. Douglas, A. Ball, and D. Ginnings, J. Res. Natl. Bur. Stand. **46**, 334 (1951).

[44]O. Kleppa, J. Chem. Phys. **18**, 1331 (1950).

[45]J. Dymond and R. Malhotra, Int. J. Thermophys. **9**, 941 (1988).

[46]F. Murnaghan, Proc. Nat. Acad. Sci. U.S.A. **30**, 244 (1944).

[47]F. Birch, J. Geophys. Res., [Solid Earth] **83**, 1257, doi:10.1029/JB083iB03p01257 (1978).

[48]M. Kumari and N. Dass, J. Phys.: Condens. Matter **2**, 3219 (1990).

[49]P. Kuchhal, R. Kumar, and N. Dass, Phys. Rev. B **55**, 8042 (1997).

[50]F. Stacey, B. Brennan, and R. Irvine, Geophys. Sur. **4**, 189 (1981).

[51]P. Vinet, J. Ferrante, J. R. Smith, and J. H. Rose, J. Phys. C: Solid State Phys. **19**, L467 (1986).

[52]H. Schlosser and J. Ferrante, Phys. Rev. B **40**, 6405 (1989).

[53]O. Schulte and W. B. Holzapfel, Phys. Rev. B **53**, 569 (1996).

[54]This value is lower than the value previously found by Okada *et al.*[61] (this value was around 4–5).

[55]L. E. Bove, F. Sacchetti, C. Petrillo, and B. Dorner, Phys. Rev. Lett. **85**, 5352 (2000).

[56]P. Thakor, Y. Sonvane, and A. Jani, Phys. Chem. Liq. **49**, 530 (2011).

[57]A. B. Coppens, R. T. Beyer, and J. Ballou, J. Acoust. Soc. Am. **41**, 1443 (1967).

[58]J. Jarzynski, Proc. Phys. Soc. **81**, 745 (1963).

[59]W. Wagner and A. Pruss, J. Phys. Chem. Ref. Data **31**, 387 (2002).

[60]N. H. Fletcher, Am. J. Phys. **42**, 487 (1974).

[61]K. Okada, A. Odawara, and M. Yao, Rev. High Pres. Sci. Technol. **7**, 736 (1998).

[62]T. Grindley and J. E. Lind, J. Chem. Phys. **54**, 3983 (1971).